Proceedings of The Second International Conference on
Vortex Methods, Sept. 26-28, 2001, Istanbul, Turkey

VORTEX METHOD MODELING OF COMPLEX, TURBULENT ENGINEERING FLOWS

Peter S. Bernard

Department of Mechanical Engineering, University of Maryland
College Park, Maryland 20742, U.S.A. /Email: bernard@eng.umd.edu

Athanassios A. Dimas

Krispin Technologies, Inc.
1370 Piccard Dr., Rockville, MD 20850, U.S.A. /Email: adimas@krispintech.com

ABSTRACT

This paper presents results from several recent simulations of turbulent flows using the VorCat code. VorCat is a commercial implementation of the gridfree vortex method that is specifically designed to treat high Reynolds number, turbulent, incompressible flows of engineering interest. Computational elements consist of straight vortex tubes combined to form filaments, and finite thickness, thin, unstructured, triangular vortex sheets, several layers deep, covering solid surfaces. The sheet mesh provides an efficient vehicle for accommodating steep vorticity gradients in the near-wall region and permits accurate evaluation of viscous diffusion and surface vorticity production. To the extent that the vortex tube elements mimic the actual tube-like vortical structures of turbulence, the efficiency and physical plausibility of the algorithm is enhanced. A de facto “subgrid" model is implemented by the use of Chorin's hairpin removal algorithm to prevent the appearance of vortices of ever diminishing scale. New vortex elements appear at the outer edge of the boundary mesh during significant ejection events. Recent applications considered here include the flow in a zero-pressure gradient boundary layer, and the flow past a multi-element airfoil at angle of attack.

1. INTRODUCTION

Vortex Methods have long been regarded as a natural approach to take for the simulation of turbulent flows: they are minimally affected by

numerical diffusion; they provide an opportunity to directly model turbulent flow through vorticity dynamics, and, by being grid-free, they are more readily applied than grid-based methods to complex geometries found in industrial applications. Moreover, with the advent of the Fast Multipole Method (FMM), vortex methods are able to simulate flows with sufficient numbers of vortex elements to accommodate turbulence. While it is not necessarily realistic to expect vortex methods to find application as a tool for Direct Numerical Simulations of turbulence, they do have sufficient resolution to qualify at the level of a Large Eddy Simulation (LES). How best to achieve this end is not self-evident; this paper considers the attributes of one particular approach toward developing a vortex method LES of turbulent flow which is the basis for the commercial VorCat code.

The form of the vortex method adopted by VorCat takes advantage of a number of special physical properties of turbulence in order to gain efficiency and accuracy. The method has been applied to several complex flows with the goal of benchmarking the level of its performance in diverse situations. Recently, computations of a zero-pressure gradient flat plate boundary layer has been undertaken for the purpose of providing stringent quantitative verification of the accuracy of the method in a standard canonical turbulent flow. Preliminary results from this study are given here including predicted mean velocity and Reynolds stresses and a qualitative analysis of the computed turbulence structure. Some results from a computation of the flow past a multi-element airfoil are also presented.

2. VORCAT ALGORITHM

The development of the VorCat code is constrained by the need to be efficient and accurate in simulating turbulent flow yet also be adaptable to the realities of commercial applications. Some guidance in how to best configure a vortex method for this end can be found by considering some of the primary physical properties of turbulence and how to best capture them numerically. In particular, the restriction to Reynolds numbers in the turbulent range suggests that viscosity will affect the flow of interest only in the near-wall region, i.e., the viscous sublayer of turbulent flow, as well as spatially intermittent regions throughout the flow where viscous energy dissipation takes place. The latter are characterized by the presence of highly stretched small-scale vorticity.

To capture these particular viscous effects, two important attributes must be imparted to the numerical scheme. First of all, the viscous sublayer adjacent to solid surfaces needs to be resolved well enough to predict viscous diffusion of vorticity from the boundary surface. Secondly, the vortex elements in the outer flow must be able to accommodate the stretching process causing the energy cascade to dissipation scales. In addressing the first of these requirements it may be noticed that the region where significant molecular vorticity diffusion occurs is largely two-dimensional in character, consisting of the accumulated regions adjacent to solid boundaries. Clearly, high aspect ratio vortex sheet elements are a natural candidate to fill out the viscous sublayer so as to provide a platform upon which to compute vorticity diffusion. It should also be noted that it is typical of engineering design analyses to provide information about the shapes of solid bodies in the form of triangularizations of the surface. This implies that a natural and efficient representation of the near-wall region should be in the form of a fixed, thin, unstructured triangular mesh of finite thickness vortex sheets. For the VorCat code the sheets are stacked normal to the surface several layers deep, with a half-thickness sheet adjacent to the boundary, and are meant to cover the viscous sublayer of turbulent wall flows, i.e., approximately no further from the wall than $y^+ = 30$. Creating such a mesh is a simple matter for even the most complicated geometries. The half-thickness sheets at the surface are assigned that vorticity necessary to enforce the no-slip condition. In particular, an image half-sheet is introduced so the surface sheet and its image do

not produce any velocity outside themselves, yet locally enforce the no-slip condition without generating a local flow normal to the solid surface.

It is not practical to have the wall vortices convect since this would unnecessarily complicate the effort at accurately computing viscous diffusion normal to the surface, e.g., extra measures would have to be taken to make sure that an adequate resolution of vortices is maintained at all times. To advance the vorticity on the mesh region, a finite volume numerical scheme for solving the 3D vorticity equation is used. If the resolution is fine enough, then wall-normal viscous diffusion with its attendant vorticity generation at the solid surface is determined with acceptable accuracy. In particular, numerical diffusion is kept within bounds so that flow at the desired Reynolds number is indeed modeled. In a further step to enhance accuracy, the vorticity on the sheets is made to be piecewise linear. This is used when computing the contributions of sheets to the velocity field.

In regards to the second viscous effect, namely, the energy dissipation occurring intermittently in turbulent flow, a useful and generally accepted model of the process assumes that energy cascades to small scales through vortex stretching. Moreover, the fine scale structure of turbulence is tube-like (1), and stretching and folding of vortex tubes takes energy to small scales (2). With this picture in mind it is natural to choose vortex tubes as the primary grid-free element of the simulation. Moreover, unlike vortex blob representations, where the vorticity amplitude can become unbounded, a tube method is unconditionally stable since the circulation is conserved during the stretching process.

In high Reynolds number flows vortex tubes stretch and fold until they approach the fine scales where viscous dissipation becomes important. Not only is it prohibitively expensive to run a vortex method calculation until such scales are populated, but it is not obvious how to correctly accommodate viscous diffusion once the tubes arrive at these scales. Fortunately, both of these pitfalls can be avoided by adopting Chorin's hairpin removal algorithm in which folded vortex pairs - as in a kink in a filament - are removed and the ends reattached (3). A conceptual basis for this procedure lies in the observation that each folded vortex tube is primarily responsible for a contribution to local energy, since the far field velocities cancel. Removal of hairpins then mimics the local dissipation process, i.e., their energy vanishes with them. If this is done, then there is no need to expend great computational resources tracking the vortex folding process until the energy reaches the viscous scales and is dissipated. In effect, the hairpin removal algorithm acts like a subgrid model, and a vortex method incorporating it has the character of a LES. The unresolved scales are those that fall below the smallest length allowed among the tube segments.

An additional benefit to the use of tubes is that they provide a direct means for representing the principal dynamical features of the near-wall region in bounded turbulent flows, i.e., the quasi-streamwise vortices which control the momentum exchange near boundaries associated with the Reynolds shear stress. It may be imagined that a tube method is the optimal means of representing the wall layer dynamics controlled by tubes. As will be illustrated below, tubes also show a significant tendency to combine together forming other kinds of vortical structures that are routinely observed in turbulent flows.

The dynamics of vortex tubes is contained in the movement of their end points and the application of rules such as hairpin removal and the subdivision of segments if they become too long. Other rules govern their creation at the outermost sheet level of the wall grid. Vorticity produced at the wall in satisfaction of the no-slip condition diffuses and convects through the mesh. To mimic the idea that new vorticity is produced in the outer flow primarily during significant ejection events from the near wall region, new vortex tubes are made to appear at the top mesh level only when the vorticity at

this location exceeds a threshold. In practical terms, this helps limit the amount of new tubes in the calculation by restricting them to those that are the most significant in the sense of containing the most energy. A description of these and other facets of the method may be found in some earlier reports, e.g., (4,5,6).

3. BOUNDARY LAYER

As a rigorous test of the VorCat code a canonical zero-pressure-gradient flat plate boundary layer has been simulated. The plate used in the simulation has a total length of 2 and a span length of 0.28. The surface is resolved by approximately 5000 triangles. In the simulations, 4 periodic images are used to enforce periodicity conditions in the spanwise direction. The flow is tripped by a bump placed at x=0.1 with height 0.003. Computed flow statistics are taken at x=1.1 which corresponds to a Reynolds number of 200,000 based on the distance from the trip.

Physical Properties

The boundary layer trip is observed to have an effect on the computed solution that agrees with current understanding of the physics of boundary layer transition and its subsequent development into a turbulent state. This is illustrated in Figs. 1 and 2 showing snapshots of the computed vortex element population from the top and side at a sequence of increasing times. Figures 3 and 4 give a magnified view of the flow from each of these perspectives. Besides the vorticity in the tubes, it should be remarked that there is considerable vorticity in the sheet mesh that is not depicted in these figures. Upstream of the boundary layer trip, there are a relatively small number of purely spanwise vortices which are typical of a laminar boundary layer. The flow in this region is clearly stable throughout the calculation, e.g., its character is unchanged in time, and the vortex elements have low vorticity amplitude.

Immediately downstream of the bump the flow remains laminar for a short distance, but is soon followed by strong transition into a highly perturbed state (where the elements are various shades of purple and magenta). This behavior is strongly reminiscent of transition in which 2D Tollmein-Schlichting waves first appear, followed by a focusing of their spanwise vorticity, which subsequently undergoes instability causing the appearance of streamwise vorticity and finally turbulence (7). Evidently, the effect of the bump is to inject vorticity outwards from the wall surface, and by so doing, accelerate the appearance of the transition process. A close-up view of the vortex elements in the latter part of the transition region shown in Fig. 5, indicates that reorientation of spanwise vorticity to the streamwise direction is associated with the presence of alternating regions of faster and slower streamwise motions, i.e., the beginnings of the streaky structure which characterizes turbulent boundary layers, and which is found to underlie the fully turbulent regions of the simulation.

The side views in Figs. 2 and 4 reveal a thickening of the boundary layer in the transition region and the generation of wall-normal vorticity. Further downstream the flow develops many structural features in the form of coherent vortices. The side images show the characteristic crumpled outer edge pattern of the boundary layer formed from individual large-scale structures. A detail of one such mushroom shaped object is shown in Fig. 6. Its appearance is identical to similar objects which are sometimes described as the “typical eddies" of the turbulent boundary layer (7). It is also noteworthy that the appearance of large-scale vortical structures in the calculation is as the end result of many individual vortex filaments undergoing collective organization into larger structures, i.e., they form naturally in the calculation, not by outside intervention.

The pictures in Figs. 1 and 2 show the spread of turbulence downstream as the flow evolves. This is clear evidence that the appearance of turbulence at this Reynolds number is attributed to the boundary layer trip. Another interesting aspect of these figures is the fingering pattern at

the leading edge of the turbulent front as the vortices convect downstream. Once the turbulent field passes a given point, then the flow thereafter remains in a state of local turbulence regeneration. The number of vortices in the calculation grows with time until vortex elements reach the downstream end of the domain and are eliminated from the computation. Fig. 7 shows the number of vortices in the calculation as a function of time, as well as the time history of the time step. After $t \approx 0.75$, the number of vortex elements increases more rapidly and the flow transitions from the initial laminar state to turbulent flow. The numerical time-step reaches a quasi-equilibrium value of about 0.0004, while the number of vortex elements starts to level off after $t \approx 2$. Note that the total number of vortex elements consists of the sum of vortex sheets and vortex tubes, where the number of vortex sheets is constant. The number of vortices indicated in the figure is for just the central panel of the foil and does not include the image panels. Thus, towards the end of this calculation there are approximately 1.5 million vortex elements contributing to the velocity field in the central region.

Turbulence statistics

A rigorous assessment of the physical correctness of the computed boundary layer depends on comparing average statistics of the predicted velocity field against measured values. For this purpose, the velocity field at the location $x = 1.1$, corresponding to $Re_x = U_\infty x/\nu = 200{,}000$ is considered. It is evident from the previous discussion that at any fixed x location it is necessary to wait until after the turbulent front has passed before collecting data with which to evaluate the turbulence statistics. At the time of this writing, the boundary layer simulation has been computed for approximately 4000 time steps with an elapsed time of 2 dimensionless units. The turbulent flow field reached the location $x = 1.1$ sometime after $t = 1$. Consequently, for the purpose of computing flow statistics, data in the time interval $1.5 < t < 2$ spaced at intervals of $\Delta t = .05$ is used.

The velocity data for computing statistics is obtained at 15 equally spaced spanwise locations at $x = 1.1$. The mean wall shear stress at this location can be used to calculate a friction velocity, U^* and with it convert all quantities to wall units, e.g., $y^+ = y\, U^*/\nu$ and $t^+ = t\, (U^*)^2/\nu$. A conversion of time to t^+ units reveals that the elapsed time interval over which the averaging has been done is approximately $\Delta t^+ = 200$, which is much smaller than previous DNS studies have shown to be necessary for fully converged velocity and Reynolds stress statistics. Thus, converged statistics are not yet available for this calculation and will have to be obtained later, after an opportunity arises to run the solution for a longer time period. Note that the simulation to time 2 has taken approximately one week of CPU time for a calculation using 64 processors.

In terms of wall units, it is also found that the typical transverse length of the sheet mesh is $\Delta z^+ \approx 80$. This is approximately 4 times larger than one would expect to be necessary to accurately represent the correct scale of the wall region structure. As a consequence, for the present simulation vortices are not placed into the flow at a fine enough scale to fully resolve the smallest scale behavior of the low speed streaks and their attendant vortices. Clearly, the results of the previous section suggest that this limitation is not enough to deprive the calculation of physical legitimacy, but it can be expected to have some effect on the mean velocity statistics. For this reason new calculations of the boundary layer will be done with a revised and improved mesh. Despite these shortcomings, it will be seen here that the predicted results give a strong signal that the physicality of the boundary layer simulation shown in the previous section is also reflected in the quantitative statistics.

First consider the mean velocity profile, U^+ displayed in Fig. 8. Also plotted is the standard log law result $U^+ = (1/.41)\, log(y^+) + 5$, the near wall relation $U^+ = y^+$, and the Spalart mean velocity DNS solution for $R_\theta = 670$ (8). The latter is appropriate since a calculation yields

that $R_\theta \approx 575$ for the VorCat simulated boundary layer at x = 1.1. It may be noted from the figure that the computed U^+ field displays a log law behavior with the correct slope, and a slight overestimation of the magnitude. It is most likely (a conjecture we hope to conclusively establish in the near future) that such quantitative discrepancies are the result of the limited sheet mesh resolution of the current simulation and the lack of sufficient time averaging. It should also be pointed out that other sources of error have yet to be fully identified, e.g., parametric studies of the effect of numerical parameters such as tube length have not been completed. Moreover, a number of enhancements to the computation of the velocity from the wall sheets are scheduled to be implemented in the near future.

A plot of the normal Reynolds stresses is shown in Figure 9. While there are some quantitative differences with the DNS solution, the degree of agreement is quite significant, particularly in view of the aforementioned resolution problem. It is clear that the magnitude of the individual stresses are well accounted for in the simulation. This means that the essential anisotropy of the turbulent boundary layer is realistically modeled. This result is all the more significant when it is realized that the Reynolds stress statistics are associated with the chaotic motion and structures in the previously described visualizations of the flow field. The most significant quantitative discrepancies in Fig. 9 are the underestimation of v_{rms} and the over-prediction of w_{rms} close to the wall surface.

The collective behavior of the normal stresses is revealed in the plot of turbulent kinetic energy shown in Fig. 10. As before, the results are suggestive of the effectiveness of the vortex method calculation. Finally, the prediction of Reynolds shear stress is also indicated in Fig. 10. The quantitative accuracy is similar to that in the normal stresses. It is significant that a definite shear stress of the correct sign and magnitude appears as part of the vortex method solution. This confirms the presence of a correct physical organization to the flow, i.e., the Reynolds stress and its attendant momentum exchange are not likely to be correctly predicted without capturing the true physical structures and their dynamics (9).

An examination of the statistics further downstream shows the development of the same trends in the data as at x = 1.1. For example, a negative Reynolds shear stress appears at any location once the turbulence passes that point. Of course, resolution continues to decrease with downstream distance, a property of boundary layers that will be addressed in subsequent computations. One other significant point is that the use of the Biot-Savart law in computing velocities is incompatible with imposing a simplified exit plane boundary condition. In fact, the absence of vorticity downstream of the plate end, affects the velocity on the nearby upstream part of the plate (10). The consequence is a tendency to exaggerate the streamwise velocities. The implication of this for the present calculation is that the boundary layer beyond approximately 1.5 experiences some acceleration that distorts the statistics. The data discussed here, at x = 1.1 is safely buffered from this part of the flow field.

4. MULTI-ELEMENT FOIL

Another application of VorCat receiving considerable attention at the present time is that of the flow past a multi-element airfoil (30P30N). To match the conditions of experimental data (11), the Reynolds number is taken to be 9 million and flow at angles of attack $\alpha = 8^o$ and $\alpha = 19^o$ are considered. The span of the foil is 1.08 and 2 periodic images are placed on either side of the main section in order to enable satisfaction of the periodicity boundary condition in the Biot-Savart calculation of velocities. In view of the high Reynolds number, the sheet mesh is very thin and thus requires a small time step to satisfy the CFL condition. Since the vortex tubes themselves do not have a similar stability requirement, their velocities can be updated according to a larger time step than that used

for advancing the vorticity field in the unstructured mesh. The resulting gain in efficiency from this technique brings the calculation of the airfoil flow to a matter of weeks instead of months. Thus, a typical foil calculation until t = 10 with $\Delta t = 0.001$ will take 2-3 weeks and have millions of vortices. At the present time, simulations of the multi-element foil have been carried out up to time $t \approx 2.2$ for both $\alpha = 8^o$ and $\alpha = 19^o$ angles of attack.

The time-step and the number of vortex elements that have been generated during the airfoil calculation are shown in Fig. 11 for the case with $\alpha = 19^o$. After about time $t \approx 1.9$, the increase in the number of vortex elements steepens and the flow transitions from the initial laminar state to a turbulent one. The vortex sheet time-step drops to a value of approximately 0.00003, while the vortex filament time-step is set to 0.0005.

A visualization of the vortex element distribution on the 30P30N foil at time $t \approx 2$ and angle of attack $\alpha = 19^o$ is displayed in Fig. 12 from a perspective above and below the airfoil. Vortex filaments are colored according to their circulation strength: red being the strongest and blue the weakest. Across the top of the main airfoil section the flow appears to be going through transition from a laminar state after entering through the forward slot. It is seen that there is increasing levels of streamwise vorticity. At the time in the image, the flow developing on the top surface is just shy of reaching the high vorticity sheet that is shedding off the sharp trailing edge of the main section. The figures suggest that the flow travels above and below the rear flap in a turbulent state.

The relatively short time since the development of turbulence in the calculation completed thus far is evident in the visualizations in Fig. 12. Clearly, it is too early to make comprehensive comparisons of the predicted turbulence statistics against experimental data. Nevertheless, some idea of the trend of the VorCat solution can be gleaned by comparing its prediction of the distribution of the pressure coefficient C_p for $\alpha = 8^o$ vs. experimental data, as shown in Fig. 13. The qualitative agreement between curves is encouraging and suggests that the VorCat solution is on track toward capturing this complex flow field.

5. CONCLUSIONS

VorCat represents one approach toward designing a vortex method for the specific goal of simulating turbulent flow. Consideration of some of the fundamental physical processes of turbulence justifies the particular use of vortex sheets and tubes in the VorCat algorithm. Some examples of the results of recent efforts at validating VorCat have been described here. Both the boundary layer and airfoil calculations appear to be on course toward establishing the qualitative and quantitative accuracy of the VorCat scheme. Final results of these studies should be reached in the near future. Extensions of this work to 3D wings or foils with partial flaps are anticipated.

With the recent award of a NIST ATP grant to VorCat, Inc., a major component of future work will be in gaining a further order of magnitude speedup in the FMM solver and in extending VorCat to include the effects of heat transfer, compressibility and combustion.

ACKNOWLEDGEMENTS

This work was funded through NASA SBIR Phase I contract number NAS1-01033 to Krispin Technologies, Inc. Computer time was provided in part by Cray, Inc.

REFERENCES

(1) Vincent, A and Meneguzzi, M. (1991). "The spatial structure and statistical properties of homogeneous turbulence," *J. Fluid Mech.* Vol. 225, pp.1-20.

(2) Chorin, A. J. (1994) *Vorticity and Turbulence*, Springer-Verlag, New York.

(3) Chorin, A. J. (1993) ``Hairpin removal in vortex interactions II,” *J. Comput. Phys.* Vol. 107, pp. 1 - 9.

(4) Bernard, P. S, Dimas, A.A. and Collins, J. P., (1999), “Turbulent flow modeling using a fast, parallel, vortex tube and sheet method," in 3rd Int’l Workshop on Vortex Flow and Related Numerical Methods, *European Series in Applied and Industrial Mathematics (ESAIM)* Vol. 7, 46-55. Editors: Giovannini, A., et al.

(5) Bernard, P. S., Dimas, A. A., Collins, P. and Lottati, I. (2000) “Large scale vortex method simulation of turbulent flow," *Proc. High Performance Computing 2000*, Ed. A. Tentner, SCS, pp. 25 - 30.

(6) Bernard, P. S., Dimas, A. and Lottati, I. (2000) “Vortex method analysis of turbulent flows" in *Vortex Methods*, Kamemoto, K. and Tsutahara, M., Eds., World Scientific, pp. 79 - 91.

(7) Van Dyke, M. (1982) *An Album of Fluid Motion*, Parabolic Press, Stanford, CA.

(8) Spalart, P.R. (1988) ``Direct simulation of a turbulent boundary layer up to Re_θ = 1410,” J. Fluid Mech. Vol. 187, pp. 61-98.

(9) Bernard, P. S., Thomas, J. M. and Handler, R. A. (1993) “Vortex dynamics and the production of Reynolds stress, *J. Fluid Mech.*, Vol. 253, pp. 385 – 419.

(10) Bernard, P. S. (1995) “A deterministic vortex sheet method for boundary layer flow," *J. Comp. Phys.*, Vol. 117, pp. 132 - 145.

(11) Chin, V. D., Peters, D. W. and Spaid, F. W. (1993) “Measurements about a multi-element airfoil at high Reynolds numbers,” Boeing Report number MDC 93K0356.

FIGURES

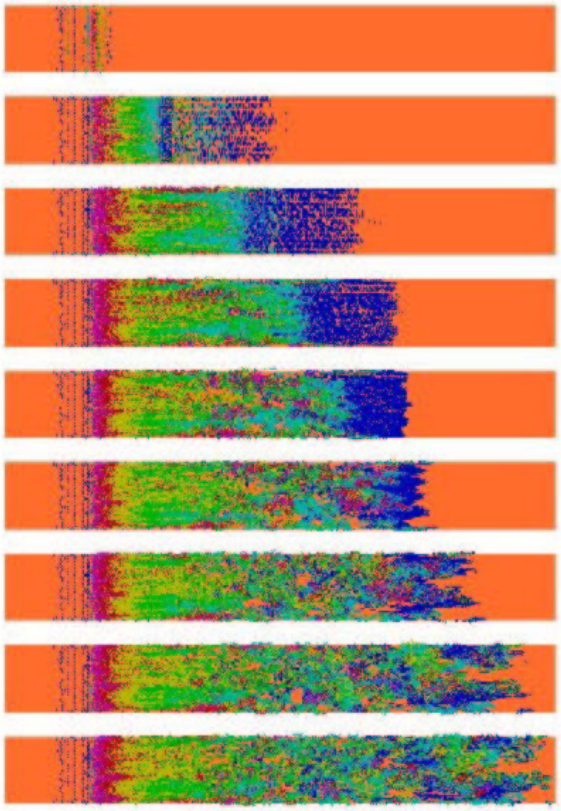

Fig. 1. Top view of the vortex filament field evolution in time (from top to bottom) for the flat-plate boundary layer at Re = 200,000.

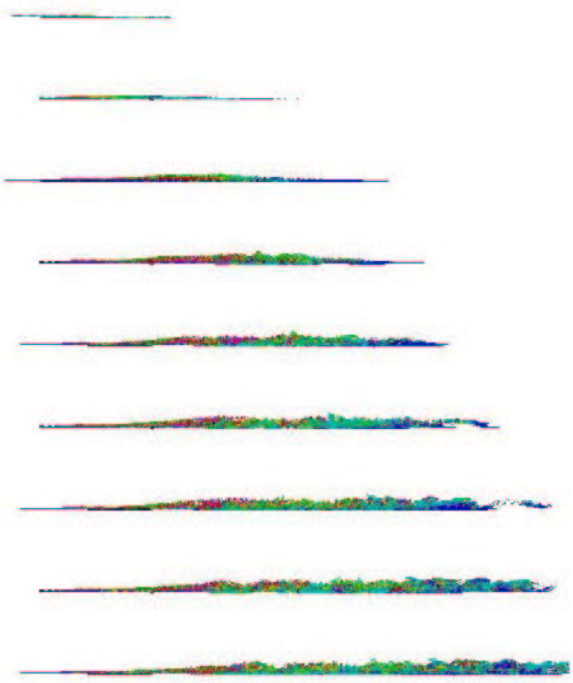

Fig. 2. Side view of the vortex filament field evolution in time (from top to bottom) for the flat-plate boundary layer at Re = 200,000.

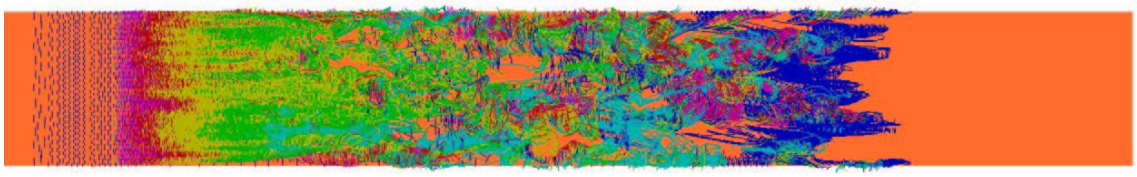

Fig. 3. Top view of the vortex filament field for the flat-plate boundary layer at Re = 200,000

Fig. 4. Side view of the vortex filament field for the flat-plate boundary layer at Re = 200,000

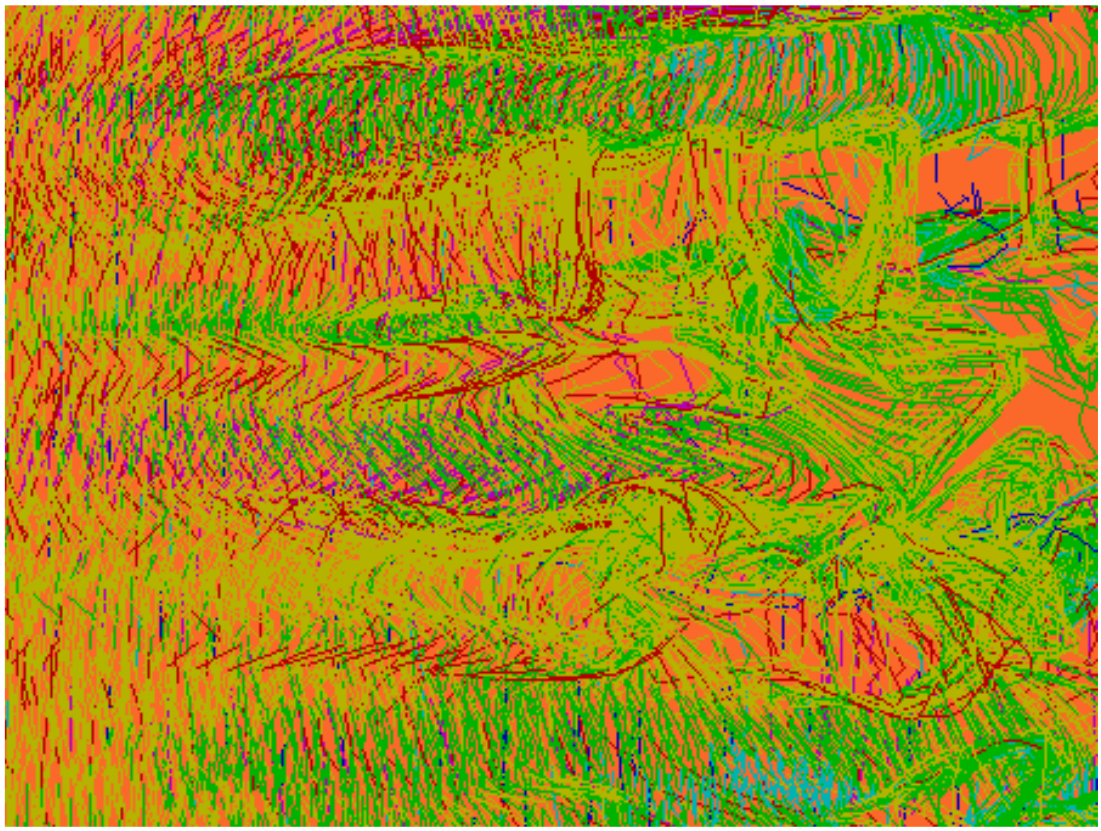

Fig. 5. Reorientation of spanwise vorticity in regions of high and low speed fluid in late transition of the turbulent boundary layer.

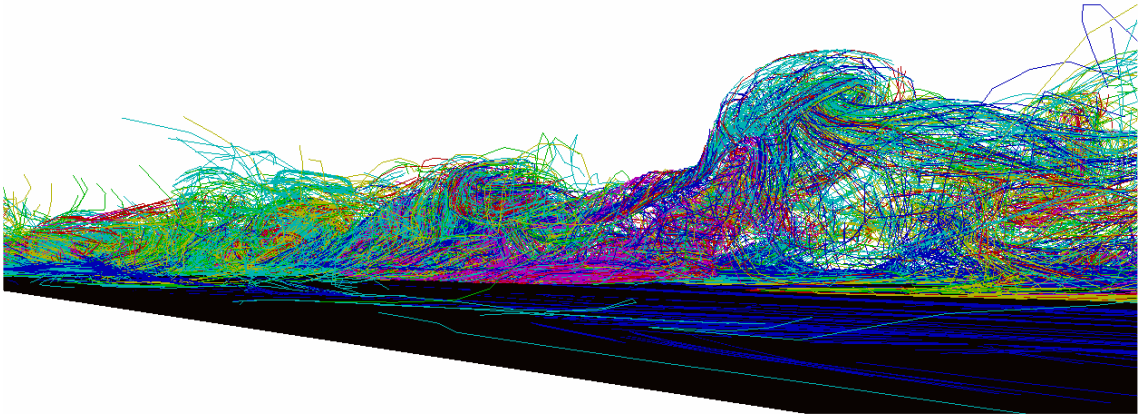

Fig. 6.Detail of “typical eddy” in the form of a mushroom-shaped vortex in the turbulent boundary layer.

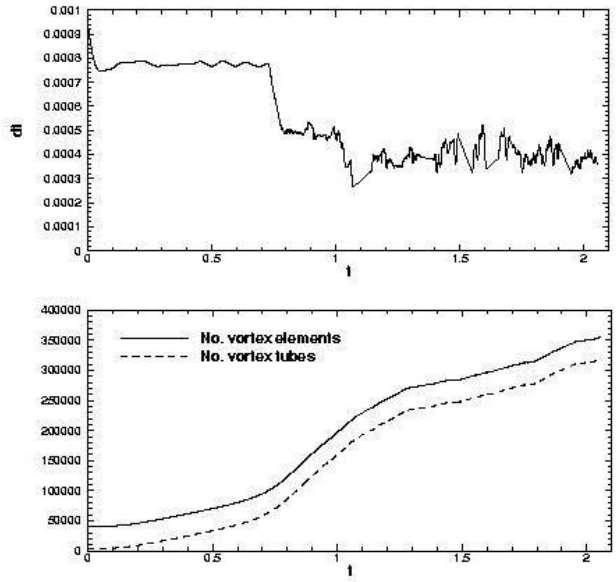

Fig. 7. Time evolution of the time-step and the number of vortex elements for the flat-plate boundary layer at Re =200,000.

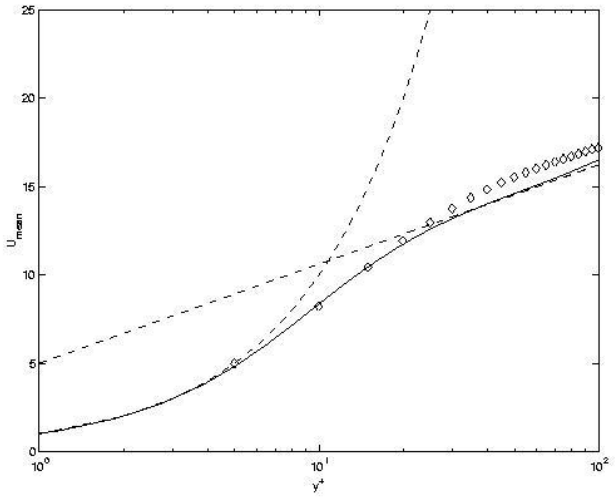

Fig. 8. Mean velocity at x = 1.1. Solid line is DNS (8); symbol is VorCat prediction.

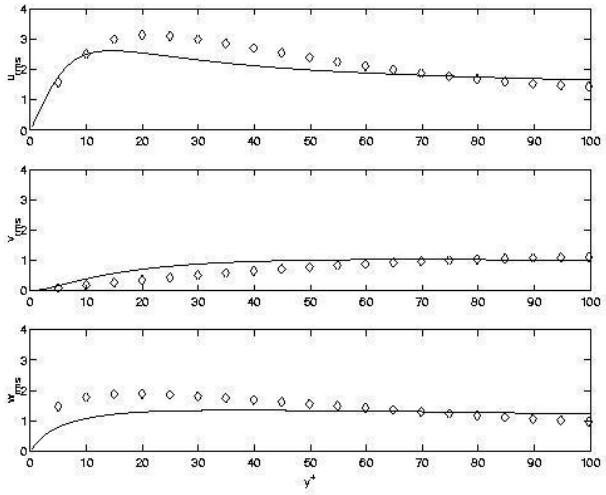

Fig. 9. Normal stresses at x = 1.1. Solid line is DNS (8); symbol is VorCat prediction.

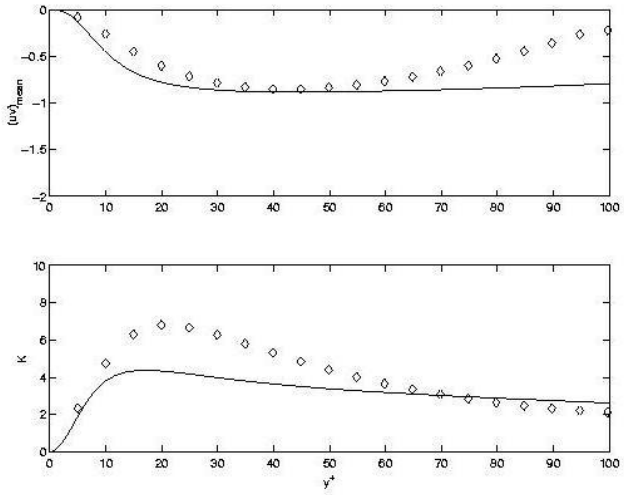

Fig. 10. Turbulent kinetic energy and Reynolds shear stress at x = 1.1. Solid line is DNS (8); symbol is VorCat prediction.

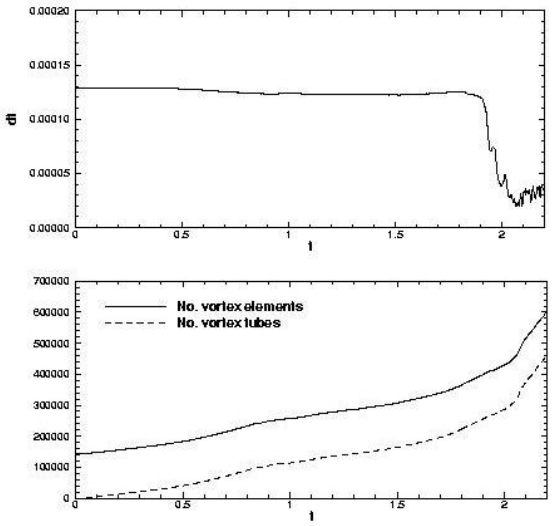

Fig. 11. Time variation of the time step and the number of vortex elements for the 30P30N foil at Re= 9 million and $\alpha = 19^o$.

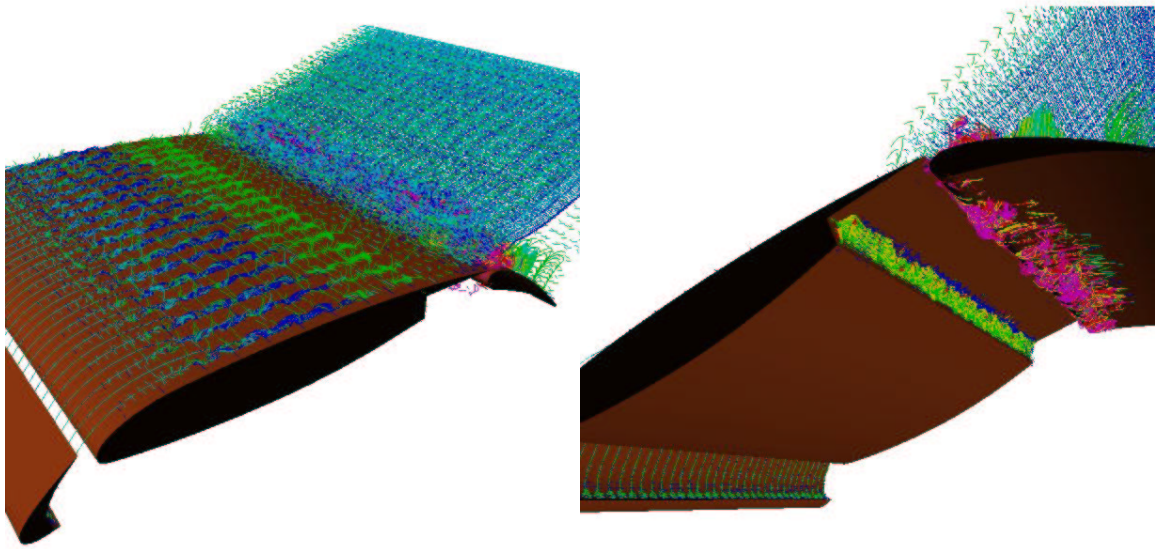

Fig. 12. Top and bottom views of the vortex filament field at t ≈ 2 for the 30P30N foil at Re = 9 million and $\alpha = 19^{o}$.

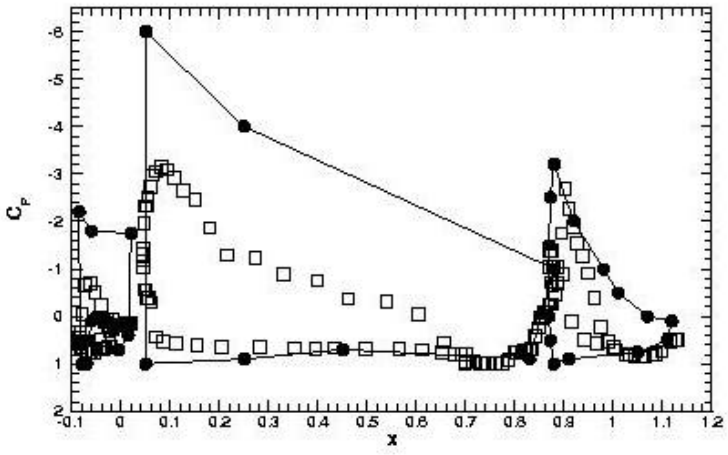

Fig. 13. The pressure coefficient distribution on the 30P30N foil at Re = 9 million and $\alpha = 8^{o}$. Solid circles correspond to experimental data; open squares correspond to VorCat predictions at time t ≈ 2.